

# <sup>7</sup>Be detection in the 2021 outburst of RS Oph

Molaro, P.<sup>1,2\*</sup>, Izzo, L.<sup>3</sup>, Selvelli, P.<sup>1</sup>, Bonifacio, P.<sup>5</sup>, Aydi, E.<sup>4</sup>, Cescutti, G.<sup>1,2,10</sup>

Guido, E.<sup>6</sup>, Harvey, E.J.<sup>7</sup>, Hernanz, M.<sup>8</sup>, Della Valle, M.<sup>9</sup>

<sup>1</sup> INAF-Osservatorio Astronomico di Trieste, Via G.B. Tiepolo 11, I-34143 Trieste, Italy

<sup>2</sup> Institute of Fundamental Physics of the Universe, Via Beirut 2, Miramare, Trieste, Italy

<sup>3</sup> DARK, Niels Bohr Institute, University of Copenhagen, Jagtvej 128, 2200 Copenhagen, Denmark

<sup>4</sup> Center for Data Intensive and Time Domain Astronomy, Department of Physics and Astronomy, Michigan State University, East Lansing, MI 48824, USA

<sup>5</sup> GEPI, Observatoire de Paris, Université PSL, CNRS, Place Jules Janssen, 92195 Meudon, France

<sup>6</sup> Telescope Live, Spaceflux Ltd, 71-75 Shelton Street, Covent Garden, London, WC2H 9JQ, UK

<sup>7</sup> Astrophysics Research Institute, Liverpool John Moores University, Liverpool, L3 5RF, UK

<sup>8</sup> Institute of Space Sciences (ICE, CSIC) and IEEC, Campus UAB, Camí de Can Magrans s/n, 08193 Cerdanyola del Valles (Barcelona), Spain

<sup>9</sup> Capodimonte Astronomical Observatory, INAF-Napoli, Salita Moiarriello 16, 80131-Napoli, Italy

<sup>10</sup> INFN, Sezione di Trieste, Via A. Valerio 2, I-34127 Trieste, Italy

<sup>11</sup> Dipartimento di Fisica, Sezione di Astronomia, Università di Trieste, Via G. B. Tiepolo 11, 34143 Trieste, Italy

Accepted.... Received 2022...

## ABSTRACT

The recurrent nova RS Oph underwent a new outburst on August 8, 2021, reaching a visible brightness of  $V = 4.8$  mag. Observations of the 2021 outburst made with the high resolution UVES spectrograph at the Kueyen-UT2 telescope of ESO-VLT in Paranal enabled detection of the possible presence of <sup>7</sup>Be freshly made in the thermonuclear runaway reactions. The <sup>7</sup>Be yields can be estimated in  $N(^7\text{Be})/N(\text{H}) = 5.7 \cdot 10^{-6}$ , which are close to the lowest yields measured in classical novae so far. <sup>7</sup>Be is short-lived and decays only into <sup>7</sup>Li. By means of a spectrum taken during the nebular phase we estimated an ejected mass of  $\approx 1.1 \cdot 10^{-5} M_{\odot}$ , providing an amount of  $\approx 4.4 \cdot 10^{-10} M_{\odot}$  of <sup>7</sup>Li created in the 2021 event. Recurrent novae of the kind of RS Oph may synthesize slightly lower amount of <sup>7</sup>Li per event as classical novae, but occur  $10^3$  times more frequently. The recurrent novae fraction is in the range of 10-30 % and they could have contributed to the making of <sup>7</sup>Li we observe today. The detection of <sup>7</sup>Be in RS Oph provides further support to the recent suggestion that novae are the most effective source of <sup>7</sup>Li in the Galaxy.

**Key words:** stars: individual: RS Oph; stars: novae – nucleosynthesis, abundances; Galaxy: evolution – abundances

## 1 INTRODUCTION

White dwarfs (WD) in close binary systems accreting H-rich matter from their companion star can explode as novae (Bode & Evans 2012; Della Valle & Izzo 2020; Chomiuk et al. 2021). All nova explosions are recurrent because the explosion does not disrupt the white dwarf and accretion is reestablished after the explosion; the recurrence periods are in general very long. However, there are about a dozen novae with more than one recorded outburst, meaning that their recurrence periods are shorter than 100 years. These are the so-called Recurrent Novae (RNe, Schaefer 2010), whereas the other novae are named Classical Novae (CNe). It is known that the companion star of the white dwarf in classical novae is a main sequence star, and the binary system is a cataclysmic variable (CV), whereas an evolved star, e.g. a red giant, is the companion of the white dwarf in a subclass of RNe, i.e., T CrB, RS Oph, V3890 Sgr and U 745 Sco (Anupama & Pavana 2020; Kato & Hachisu 2012). Recurrence periods as short as decades imply higher mass-transfer rates onto the white dwarf and higher white dwarf masses close to the Chandrasekhar mass limit in

RNe than in CNe. Therefore, RNe are considered good scenarios of type Ia supernova explosions (Livio & Turan 1992; Schaefer 2010; Mikołajewska & Shara 2017), and this has been suggested also for RS Oph (Hachisu & Kato 2001; Hernanz & José 2008). However, there is evidence that not all RNe may end up their life as a type-Ia SN (Selvelli et al. 2008).

The RN RS Oph comprises a white dwarf with mass of 1.2-1.4  $M_{\odot}$  close to the Chandrasekhar limit and a K4-M0 red giant with a relatively small mass of about 0.68-0.80  $M_{\odot}$  revolving with a period of  $453.6 \pm 0.3$  d (Brandi et al. 2009; Mikołajewska & Shara 2017). The outbursts result from a hydrogen thermonuclear runaway (TNR) on the white dwarf surface as a consequence of mass transfer from the red giant. Five historical outbursts have been recorded over a century providing a frequency of once every 15-20 years. The more recent ones which occurred in 1985 and 2006 have been intensively studied with observations ranging from X-ray to radio wavelengths, and covering all phases from quiescence to outburst (Evans et al. 2008).

The mechanism of the explosion is the same as in classical novae (CN). The H-rich accreted material on top of WD grows until it reaches conditions at its bottom to ignite H under degenerate conditions, first through the p-p chains and later - when  $T > 2 \times 10^7$  K -

\* E-mail: paolo.molaro@inaf.it

† Based on data from Paranal Observatory, ESO, Chile

through the CNO cycle. Nuclear burning proceeds fast and without control, since degeneracy prevents expansion of the envelope, thus leading to a TNR. Some beta-unstable nuclei produced by the CNO cycle are transported by convection to the outer envelope, where they decay, releasing energy that leads to the expansion and ejection of matter at velocities of several thousands of  $\text{km s}^{-1}$  with a simultaneous brightening by several magnitudes (Gallagher & Starrfield 1978).

Arnould & Norgaard 1975 and Starrfield et al. 1978 suggested that in the thermonuclear process, a mechanism similar to that one proposed by Cameron and Fowler to explain the  $^7\text{Li}$  rich giants (Cameron 1955; Cameron & Fowler 1971) could take place. The reaction  $^3\text{He}(\alpha, \gamma)^7\text{Be}$  leads to the formation of  $^7\text{Be}$  which, if transported by convection to cooler zones with a time-scale shorter than its electron capture time, survives from destruction. This suggestion was quantitatively elaborated by Hernanz et al. (1996); José & Hernanz (1998) but was thwarted by the non-detection of  $^7\text{Li}$  in the outburst spectra of CN (Friedjung 1979). After decades of observational failures, the possible presence of  $^7\text{Li}$  670.8 nm resonance line was reported in nova V1369 Cen (Izzo et al. 2015), and the parent nucleus  $^7\text{Be}$  was recognized in several CN (Tajitsu et al. 2015, 2016; Molaro et al. 2016; Izzo et al. 2018; Selvelli et al. 2018; Molaro et al. 2020; Arai et al. 2021; Molaro et al. 2021).  $^7\text{Be}$  is short-lived (53 d) and its presence in the outburst spectra implies that it has been freshly created in the TNR processes of the nova event. The general non-detection of neutral  $^7\text{Li}$  in CNe could be explained considering that  $^7\text{Be}$  decays with a capture of an internal K-electron and therefore ends up as ionized lithium whose ground-state transitions are outside the optical range and are not observable (Molaro et al. 2016).  $^7\text{Be}$  decays into an excited  $^7\text{Li}$  state that de-excites to the ground state producing high-energy photons at 478 keV (Clayton 1981; Gomez-Gomar et al. 1998). Several attempts to detect the 478 keV line with Gamma-ray satellites have been unsuccessful, but the limits derived are consistent with the expected emission values (Harris et al. 2001; Jean et al. 2000; Siebert et al. 2018, 2021).

The astrophysical origin of Galactic lithium still represents an open question (Fields 2011). The  $^7\text{Li}$  abundance today is much higher than the primordial value. This requires the existence of one or several sources which are not yet identified. Spallation processes in the interstellar medium is an established source but its contribution cannot be higher than 10% (Davids et al. 1970). Stellar sources such as AGB stars, red giants and/or supernovae have been suggested to be actively producing lithium (Romano et al. 2001). The recent yields measured in CNe imply a  $^7\text{Li}$  over-production by up to four orders of magnitude greater than meteoritic and therefore CNe alone could make up most of the Galactic  $^7\text{Li}$  (Molaro et al. 2016; Cescutti & Molaro 2019; Molaro et al. 2020, 2021).

## 2 THE 2021 OUTBURST

The most recent RS Oph eruption occurred on 2021 Aug 08.50 ( $\pm 0.01$ ), or 2459434.50 MJD, reaching a maximum V-band magnitude of 4.8 on 2021 Aug 09.58 ( $\pm 0.05$ ), or 2459435.68 MJD (Munari & Valisa 2021). Basic information on the RS Oph system is summarized in Tab 1. The parallax of RS Oph has been measured by Gaia (Gaia Collaboration et al. 2021):  $0.373 \pm 0.023$  mas. Bailer-Jones et al. (2021) have provided geometric and photogeometric distances for almost 1.5 billions stars in the Gaia EDR3 catalogue. Both these values, as well as the lower and upper limits to these distances are provided in Table 1. The Gaia parallax has to be corrected for the zero point (Lindgren et al. 2021), providing 0.416 mas. A direct in-

**Table 1.** RS Oph: basic data (to be completed). References: 1) a Brandi et al. (2009), 2. Gaia Collaboration et al. (2021), 3. Bailer-Jones et al. (2021)

Property	Value	Ref
System	WD+M2IIIpe	1
Period	$453.6 \pm 0.4$ d	1
RA	17 50 13.20	
DEC	-06 42 28.5	
Parallax	$0.416 \pm 0.023$	2
Distance	$2404 \pm 160$ pc	2
Geometric distance	2402 pc	2276 – 2524 pc
Photogeometric distance	2441 pc	2219 – 2650 pc
G (EDR3)	$10.43 \pm 0.010$	3

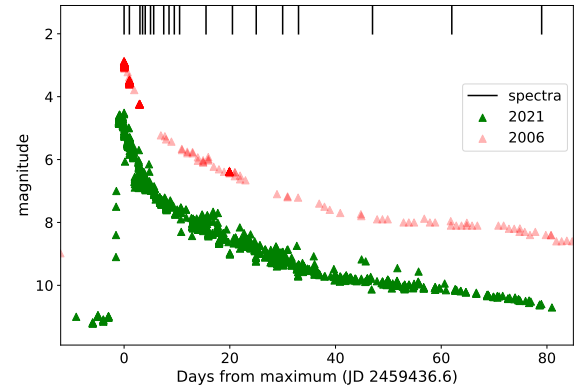


**Figure 1.** The V-band light curve of RS Oph as obtained by AAVSO members during the last outburst (green data) and the previous one in 2006 (red). Black lines mark the epochs of our spectral campaign.

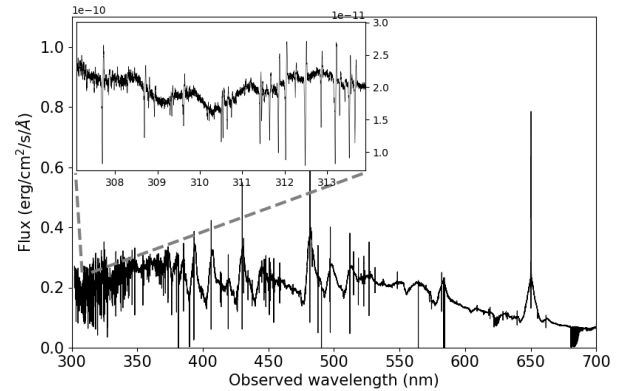


**Figure 2.** Optical de-reddened spectrum 1.6 day after explosion (MJD 59434.47). Broad P Cygni profiles of Balmer H I, He I, Fe II, and Na I, dominate the spectrum. Narrow P Cygni components are superimposed to the broad emission lines of the nova outburst components originating in the wind of the red giant. Towards the blue end they are so numerous that they mimic a noisy spectrum. The small portion in the  $^7\text{Be}$  regions is zoomed in the inset showing the lines of the wind from the giant whose identifications are reported in Tab 2.

**Table 2.** Journal of observations in August 2021. The RS Oph explosion is taken in 2459434.50 MJD, or 2021 Aug 08.50 ( $\pm 0.01$ ) (Munari & Valisa 2021). The values of the Cross Disperser specify the wavelength of UVES central setting: CD1=346.0 nm, CD3=580.0 nm, CD2=437.0 nm and CD4=760.0 nm. MJD refers to the start of the exposure. We also include the last observation of 29 March 2022 used for the nebular phase.

Epoch	Inst	Date MJD 2400000	Grism	slit	exp sec	airmass	DIMM arcsec
1	UVES	59436.0743	CD3	0.4	10	1.059	0.60
9-Aug		59436.0743	CD1	0.4	60	1.059	0.60
1.6 d		59436.0750	CD3	0.4	10	1.059	0.55
		59436.0757	CD3	0.4	10	1.060	0.57
		59436.0763	CD3	0.4	10	1.061	0.59
		59436.0789	CD4	0.3	15	1.063	0.66
		59436.0789	CD2	0.3	15	1.063	0.66
2	UVES	59437.0211	CD3	0.6	5	1.069	0.50
10-Aug		59437.0211	CD1	0.6	30	1.069	0.50
2.5 d		59437.0217	CD3	0.6	5	1.069	0.50
		59437.0287	CD3	0.6	2	1.061	0.45
		59437.0288	CD1	0.6	15	1.061	0.45
		59437.0293	CD3	0.6	2	1.061	0.47
		59437.0339	CD4	0.6	2	1.057	0.46
		59437.0339	CD2	0.6	5	1.057	0.46
3	UVES	59439.2151	CD1	0.4	360	2.049	0.53
12-Aug		59439.2163	CD3	0.4	60	2.075	0.56
4.7 d		59439.2176	CD3	0.4	60	2.103	0.61
		59439.2221	CD4	0.3	60	2.208	0.67
		59439.2221	CD2	0.3	60	2.208	0.67
4	HARPSN	59439.8703	HR		300	1.242	
13-Aug			HR		300	1.242	
5.3 d			HR		300	1.242	
5	UVES	59440.2081	CD3	0.4	60	1.965	1.23
13-Aug		59440.2081	CD1	0.4	360	1.965	1.23
5.7		59440.2094	CD3	0.4	60	1.990	1.23
		59440.210	CD3	0.4	60	2.014	1.23
		59440.2147	CD4	0.3	60	2.100	1.82
		59440.2147	CD2	0.3	60	2.100	1.82
6	UVES	59441.2152	CD3	0.4	120	2.173	2.28
14-Aug		59441.2152	CD1	0.4	480	2.173	2.28
6.7 d		59441.2171	CD3	0.4	120	2.221	1.95
		59441.2191	CD3	0.4	120	2.272	2.25
		59441.2228	CD4	0.3	120	2.372	2.25
		59441.2228	CD2	0.3	120	2.372	2.25
7	FIES	59441.9051	HR		300	1.230	
15-Aug			HR		300	1.230	
7.4 d			HR		300	1.230	
8	HARPSN	59443.9280			300	1.282	
17-Aug					300	1.282	
9.5 d					300	1.282	
9	UVES	59444.9656	CD3	0.6	120	1.137	1.79
18-Aug		59444.9656	CD1	0.6	480	1.137	1.79
10.5 d		59444.9675	CD3	0.6	120	1.132	1.67
		59444.9695	CD3	0.6	120	1.127	1.69
		59444.9735	CD4	0.3	120	1.116	1.79
		59444.9735	CD2	0.3	120	1.116	1.79
10	FIES	59445.8997	HR		360	1.235	
19-Aug			HR		360	1.235	
11.4 d			HR		360	1.235	
11	UVES	59447.0107	CD3	0.6	120	1.054	0.99
20-Aug		59447.0108	CD1	0.6	480	1.054	0.99
12.5 d		59447.0146	CD3	0.6	120	1.053	0.90
		59447.0188	CD3	0.6	60	1.051	0.77
		59447.0205	CD3	0.6	30	1.051	1.01
		59447.0205	CD1	0.6	90	1.051	1.01
		59447.0214	CD3	0.6	30	1.051	0.92
		59447.0223	CD3	0.6	30	1.051	0.96
		59447.0273	CD4	0.3	120	1.051	1.34
		59447.0274	CD2	0.3	120	1.051	1.34
		59447.0303	CD4	0.3	30	1.052	1.42
		59447.0303	CD2	0.3	30	1.052	1.42
	UVES	59457.0385	CD3	0.6	120	1.086	0.87
31-Aug		59457.0385	CD1	0.6	480	1.086	0.87
20.5 d		59457.0405	CD3	0.6	120	1.089	1.13
		59457.0424	CD4	0.6	120	1.103	0.84
		59457.0471	CD2	0.6	120	1.103	0.84
	UVES	59667.2807	CD1	3.0	240	1.584	0.51
29 March		59667.2826	CD3	3.0	120	1.584	0.50
232.8		59667.2939	CD4	3.0	400	1.472	0.42
		59667.2940	CD2	3.0	400	1.472	0.42

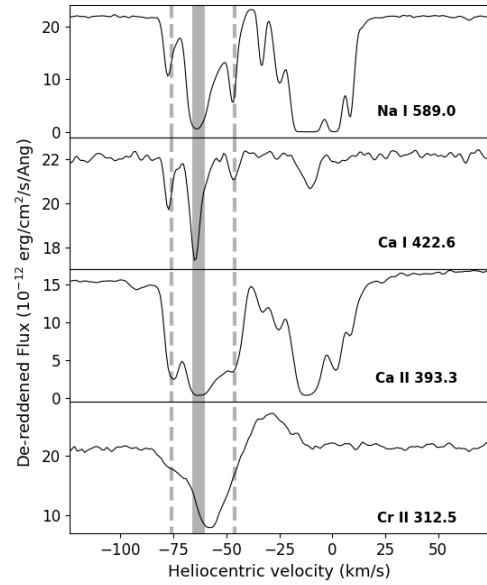


**Figure 3.** Spectra of day 1.5 of Na I 588.995 nm, Ca I 422.6728 nm, and Ca II 393.3663 nm showing the red-giant wind and the interstellar medium structure. Velocities are heliocentric corrected. The systemic velocity for the RS Oph system is  $-40.2 \text{ km s}^{-1}$  (Fekel et al. 2000), and therefore the main component of the red giant wind is expanding with a velocity of about  $-23 \text{ km s}^{-1}$  in the RS Oph rest frame while the two satellite ones at  $\pm 15 \text{ km s}^{-1}$  with respect the main component result from the orbital motion (dashed lines). The Cr II 312.5 nm line is shown as example of the lines from the circumstellar material produced by the red-giant wind and excited by the nova UV-flash.

version of this parallax provides a distance of  $(2.40 \pm 0.16) \text{ kpc}$ . The parallax measurement is disturbed by the motion of the photocentre, due to the orbital motion of the system as shown by the astrometric excess noise that is 0.13 mas. A much better measurement of the parallax will be provided at the end of the Gaia mission, where also the astrometric orbit shall be solved. Yet, Gaia EDR3 provides data that have been taken in almost 4 years (25 July 2014 to 28 May 2017), thus averaging this motion over more than three orbits, implying that the parallax should be accurate, within the stated error. It is significant that all three distance estimates (by parallax inversion, geometric with prior and photogeometric with prior) are consistent, within errors, with the distance derived from the expansion velocity of the shells by Rupen et al. (2008) that has been suggested to be the best distance estimate of RS Oph by MAGIC Collaboration et al. (2022).

The 2021 outbursts displayed a rapid rise in brightness reaching about 5th magnitude within 24 hours from a pre-burst magnitude of 12.5 in the *B* band<sup>1</sup>. The following photometric behaviour was very similar to previous outbursts as shown in Fig. 1. The behaviour shows fast decline at the beginning and slowing down during a second phase. The outburst was detected all across the electromagnetic spectrum from radio (Sokolovsky et al. 2021a,b) to X-rays (Enoto et al. 2021a,b; Ferrigno et al. 2021; Luna et al. 2021; Page et al. 2021; Page 2021; Rout et al. 2021; Shidatsu et al. 2021), gamma-rays (Cheung et al. 2021a,b; MAGIC Collaboration et al. 2022) at GeV energies

<sup>1</sup> <https://www.aavso.org/>

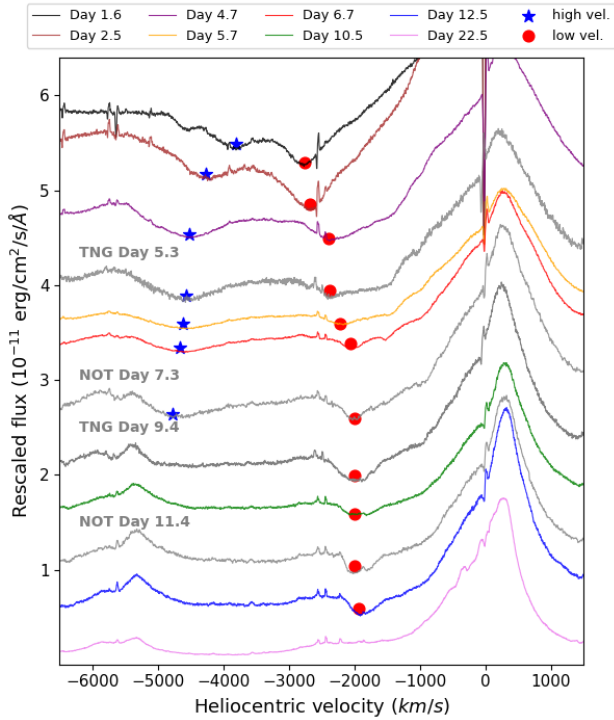


**Figure 4.** The absorption in  $H_{\delta}$  410.1735 nm in the outburst ejecta showing several components and their evolution, top to bottom, in the first 23 days after explosion. The narrow P-Cygni feature with the absorption centered at  $-63.4 \text{ km s}^{-1}$  is the  $H_{\delta}$  line of the red-giant wind. Note the  $\text{He I}$  402.6 nm emission line growing after day 10 at approximate position of  $-5300 \text{ km s}^{-1}$  in the figure. The data show spectra taken with UVES at the VLT with different colors, while spectra obtained with HARPS-N at the TNG, and with FIES at the NOT are plotted in gray. The high- and low-velocity components, as explained in the main text, are reported with blue stars and red circles, respectively.

and, for the first time, even at TeV energies (Wagner & H. E. S. S. Collaboration 2021a,b). Search for neutrino emission with IceCube was negative (Pizzuto et al. 2021). The radio emission is largely nonthermal (Sokolovsky et al. 2021b). An inverted spectrum shape that was observed early in the eruption was produced by external free-free absorption or synchrotron self-absorption within the radio emitting region. A nearly flat spectrum together with deviations from a simple power law fit are observed at later times indicating that the emitting region is inhomogeneous or remains partly hidden behind some absorbing material.

The spectra of RS Oph were obtained at VLT/UVES by triggering an ESO ToO program (Prog. ID: 105.D-0188, PI P. Molaro), after the alert with the earliest optical spectrum taken at MJD 59436.07427, or 1.6 days after explosion. The settings used were DIC1 346-564, with ranges 305-388 nm and 460-665 nm, and DIC2 437-760 with ranges 360-480 nm and 600-800 nm in the blue and red arms, respectively. The journal of the observations for the nova is provided in Table 2. The nominal resolving power of early spectra was of  $R = \lambda/\delta\lambda \approx 100,000$  for the blue arm setting the slit at 0.4 arcsec and  $\approx 130,000$  for the red arm for a slit of 0.3 arcsec. In late spectra the slit was set to 0.6 arcsec for the blue arm to cope with the nova fading in the blue providing a uniform  $R = \lambda/\delta\lambda \approx 66,000$  in both arms.

The actual slits used are provided in Table 2. Overlapping spectra were combined for each epoch to maximise the signal-to-noise ratio. The spectra have been carefully cleaned from the telluric  $\text{O}_3$  Huggins bands by means of a B-type subdwarf HD 149382 (Schachter 1991). Few spectra were also obtained with HARPS-N, The High Accuracy Radial velocity Planet Searcher for the Northern hemisphere (Cosentino et al. 2012) (Prog. ID: A43-TAC20 and A44-TAC17, PI: Izzo) at the 3.6m Telescopio Nazionale Galileo (TNG) and with FIES, the high resolution Fiber-fed Echelle Spectrograph (Telting et al. 2014), at the 2.5 m Nordic Optical Telescope (NOT), both at La Palma, Spain (Prog. ID: 63-013, PI: Izzo). The spectral range of the HARPS-N is from 383 nm to 693 nm with a  $R = \lambda/\delta\lambda \approx 120,000$ . For FIES the spectral coverage is 400-830 nm with a  $R = \lambda/\delta\lambda \approx 65,000$ . The spectra have been flux calibrated by means of spectroscopic standards and corrected for a reddening of  $E(B - V) = 0.73$  (Cassatella et al. 1985; Snijders 1987). The flux calibration for the late, nebular spectra has been refined using photometry from AAVSO (Kafka 2021).

A portion of the first optical spectrum from 300 to 700 nm is shown in Fig. 2. Broad P-Cygni profiles of Balmer  $H_I$ , Fe II, O I, and Na I, along with weaker, broad lines of He I and dominate the spectrum. The Fe II multiplet 42 is the main contributor to the emission features at 492.4, 501.8, and 516.9 nm. In Fig 4 the several absorption components and their evolution in the  $H_{\delta}$  410.1735 nm are shown. The blue edge of hydrogen absorption shows a maximum terminal velocity of the ejecta of  $\sim -4700 \text{ km s}^{-1}$  on day 1.6, which then accelerates to  $\sim -5200 \text{ km s}^{-1}$  at day 2.5 and remains constant afterwards. This is a quite different behavior from what described in MAGIC Collaboration et al. (2022) where the terminal velocity is taken to reach  $-4200 \pm 250 \text{ km s}^{-1}$  with a notable decrease to about  $-2000 \text{ km s}^{-1}$  around day 4. As it is possible to see in Fig 4 the component at about  $-2000 \text{ km s}^{-1}$  was present since the beginning of the outburst and does not result from a decrease of the high velocity component. Tatischeff & Hernanz (2007) from the analysis of the X-ray and IR observations of the RS Oph 2006 eruption predicted that a recurrent nova with a red giant companion can indeed accelerate protons and electrons, as now has been suggested by high-energy detection (MAGIC Collaboration et al. 2022; H. E. S. S. Collaboration et al. 2022).

The broad emission lines are shrinking and  $H_{\alpha}$  becomes highly non-Gaussian revealing a signature of bipolar flow. An expanding bipolar structure was detected after the 2006 eruption in the E-W direction and a similar circumstance could occur also for that of 2021 (Ribeiro et al. 2009; Montez et al. 2021). A detailed description of spectral evolution will be given elsewhere.

Narrow P-Cygni components which originate in the wind of the red giant are superimposed to the broad emission lines of the nova outburst. In Fig. 3 are shown the spectral regions of Na I, Ca I, Ca II K, and  $^7\text{Li I}$ , showing the red-giant wind and the interstellar medium structure. The Na I lines show red-giant wind absorption components at  $-48$ ,  $-63$ , and  $-77 \text{ km s}^{-1}$ . The stronger central component at  $-63 \text{ km s}^{-1}$  and the two satellite ones result from the systemic orbital motion which has an amplitude of about  $30 \text{ km s}^{-1}$ . The systemic velocity for the RS Oph system is  $-40.2 \text{ km s}^{-1}$  (Fekel et al. 2000), therefore the wind is expanding with a velocity of about  $-23 \text{ km s}^{-1}$  in the RS Oph rest frame. In fact, the wind velocities of the red giant wind measured in the recent outburst are very close to those measured in the 2006 outburst and in quiescence (Patat et al. 2011). A few lines falling in the Be II and Na I regions together with their velocities are reported in Tab. 2. These lines form in the circumstellar material produced by the red-giant wind and are excited by the nova UV-flash. They only show evidence of the main central component seen as a P-Cygni profile. It is plausible that the slow red-giant wind filled up



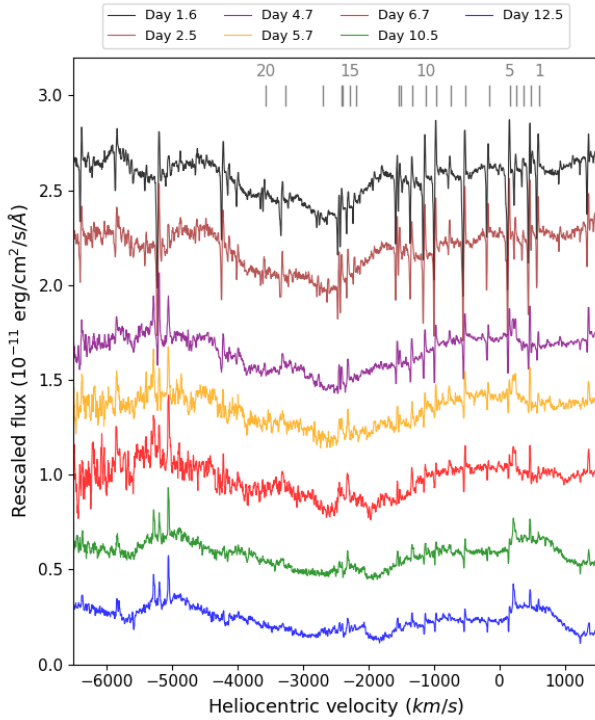


**Figure 5.** As in the previous figure but for the  ${}^7\text{Be}$  region. The zero in the x-axis is taken at 313.0583 nm. Spectra are corrected for an extinction of  $E(B-V)=0.73$  and for  $\text{O}_3$  absorption. The spectra show the complex absorption due to the outburst ejecta and the narrow P-Cygni lines of the red-giant wind which are identified in Tab. 2. The  $\text{O III } 313.37$  nm begins to be seen in emission in the last spectra at slightly positive velocities.

the cavity created by the previous explosions and in particular by that of 2006.

### 3 ${}^7\text{Be}$ DETECTION & ABUNDANCE

The UVES, HARPS-N and FIES spectra covering the  $\text{H}\delta$  are shown in Fig. 4 for the first 11 epochs of our observations. Besides emissions, the outburst hydrogen spectra show broad absorption in a range of radial velocities spanning from  $-1000$  to  $-5000 \text{ km s}^{-1}$ . There are two broad absorption features with central velocities at about  $-2800 \text{ km s}^{-1}$  and  $-3800 \text{ km s}^{-1}$  that show some variation in radial velocities from day 1.5 to day 12.5. To note the  $\text{He I } 402.6 \text{ nm}$  emission at about  $-5200 \text{ km s}^{-1}$  which is growing up in the last four spectra of the sequence. The next spectrum is on the 30 August, or day 22.5 after explosion, where all the absorption components present in the Balmer lines are no longer visible, either because they weakened or because they are hidden in the plethora of emission lines developed by the nova. The corresponding UVES spectra centered onto the  ${}^7\text{Be } 313.0 \text{ nm}$  region are shown in Fig. 5 revealing a quite complex behaviour. The narrow P-Cygni lines of the red-giant wind falling in this restricted spectral portion are identified and measured in Tab. 2. To note that while the  $\text{Cr II}$  lines maintain a P-Cygni profile the  $\text{Fe II}$  from day 5 onwards are seen only in emission. This is because the  $\text{Cr II}$  are formed from transitions which start from metastable levels

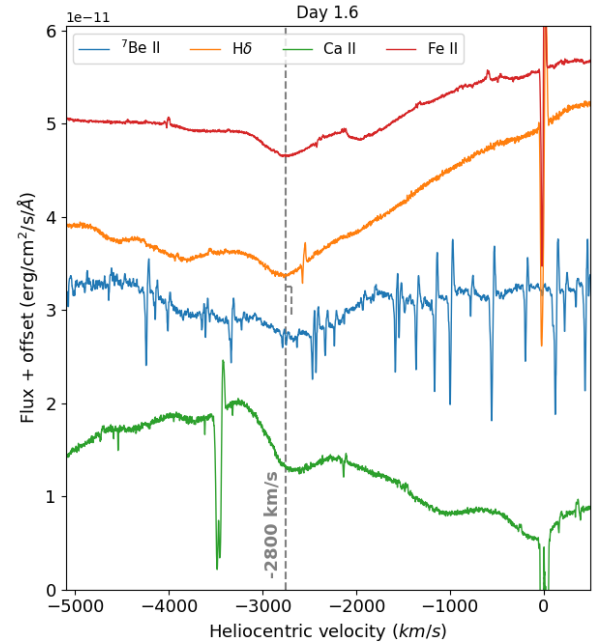


**Figure 6.** Spectra of  ${}^7\text{Be}$  together with  $\text{H}\delta$ ,  $\text{Ca II K}$  and  $\text{Fe II } 516.903$  at day 1.6 plotted on a common velocity scale. For  ${}^7\text{Be}$  the zero of the scale is at 313.0583 nm. The emission falling in the middle of the  $\text{Ca II K}$  spectrum is  $\text{H I } 388.905 \text{ nm}$  and the two absorptions at  $\approx -100$  and  $\approx -1100 \text{ km s}^{-1}$  are the components at  $-2800$  and  $-3800 \text{ km s}^{-1}$  of  $\text{Ca II H}$  and  $\text{H I } \epsilon$  lines, respectively.

at about 2.46 eV, while those of  $\text{Fe II}$  originate from non-metastable levels with an higher energy of about 3.9 eV. Thus, when radiation drops they are depopulated earlier with a corresponding reduction or suppression of the absorption. To note that the  $\text{O III}$  line at 313.37 nm appears in emission in from Day 12.5, as shown in Fig 5.

Fig. 6 shows the  ${}^7\text{Be}$  spectra of day 1.5 along with the portions of  $\text{Ca II K}$ ,  $\text{Fe II}$  and  $\text{H}\delta$  lines on a common velocity scale.  $\text{H}\delta$  is adopted as representative of the absorption seen in hydrogen being the less blended and still relatively strong.  $\text{Ca II H}$  cannot be used since it is contaminated with  $\text{H}\epsilon$  and also with the Galactic interstellar components of  $\text{Ca II K}$ . To note that the hydrogen line  $\text{H I } 388.905$  is falling in the middle of the  $\text{Ca II K}$  absorption and shows a P-Cygni profile with narrow absorption and narrow emission. The  $\text{He I } 388.8605, 388.8646, 388.8649 \text{ nm}$  lines are also present with the probable emission suppressed by the  $\text{H I}$  absorption falling on the same position. A common broad absorption with central velocity of about  $-2800 \text{ km s}^{-1}$  is present in all species, and possibly also one at  $\approx -3800 \text{ km s}^{-1}$ . The vertical lines in the figure mark the  ${}^7\text{Be II}$  doublet at  $\lambda 313.0583 + \lambda 313.1228$  doublet which has a separation of  $62 \text{ km s}^{-1}$ . To note that the  $-3800 \text{ km s}^{-1}$  is absent in the very early spectrum at MJD 59435.46, or 0.96 days after explosion, of Taguchi et al. (2021). The faster component at  $-3800 \text{ km s}^{-1}$  appears only over than half a day later. This is something common in classical novae, where we see slow, pre-maximum P Cygni profiles, followed by faster components that are delayed by a few hours to a few days (Aydi et al. 2020). Aydi et al. (2020) interpreted low velocity components of typically few hundreds  $\text{km s}^{-1}$ , originating in a slow, early ejection, and the fast component is a faster wind driven by residual

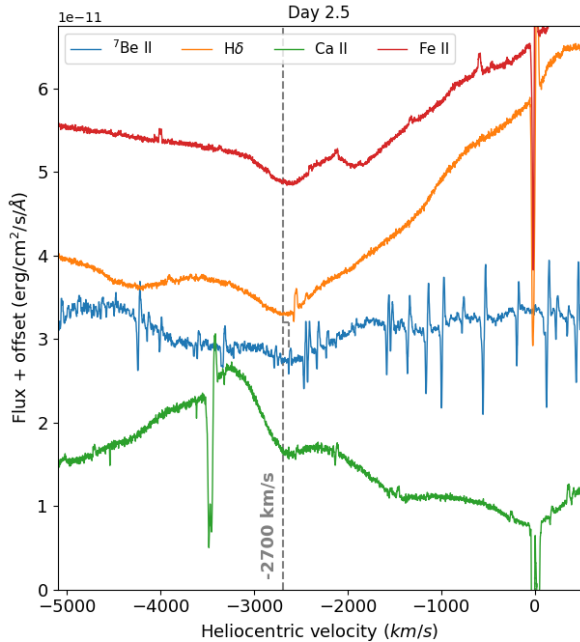


**Figure 7.** As in the previous figure for day 2.5. To note the enhancement of the emission of the H I 388.905 nm falling in the middle of the Ca II K absorption.

nuclear burning and expanding at velocities of thousands of  $\text{km s}^{-1}$ . Unfortunately, in the RS Oph spectra there is no evidence of narrow components in the outburst absorptions at any available epoch, which would reveal the  $^7\text{Be}$  doublet structure clearly demonstrating the presence of  $^7\text{Be}$ . Thus, the identification with  $^7\text{Be II}$  313.0 nm relies only on the similarity of line profile and on the absence of alternative significant blends as it has been discussed in other studies (Tajitsu et al. 2015; Molaro et al. 2016). Fig. 7 shows the same transitions at day 2.5. The hydrogen line H I 388.905 nm develops a strong emission which modifies significantly the Ca II K absorption profile. Close correspondence persists for the  $-2800 \text{ km s}^{-1}$  velocity component which is marginally affected by the emission. By day 4.7 the absorptions of metal components are gone. Interestingly, the features attributed to  $^7\text{Be}$  remain there, which implies that the absorptions cannot be made of a blend of metallic lines. At this epoch the highest velocity component in hydrogen lines showed an acceleration, but the correspondence with the analog  $^7\text{Be}$  absorption is lost. This could be the result of the shock wave following the interaction of the expanding ejecta with the circumstellar material created by the wind of the red-giant and the subsequent proton acceleration (MAGIC Collaboration et al. 2022). The velocity coherence with hydrogen is recovered when a component shows up at  $\approx -1900 \text{ km s}^{-1}$  in the spectra after days 6.7. This component is possibly the  $-2800 \text{ km s}^{-1}$  decelerated by the collision between high velocity gas of the outburst and the circumstellar material created by the red giant wind since the 2006 explosion. H $\delta$  and  $^7\text{Be}$  of the last two epochs are shown in Fig 8 and 9 together with O I which is the only element strong enough to be seen in absorption. The profiles of the new component are very similar and are suggestive of the presence of a common absorption at these velocities.

The resonance Ca II K line is required to estimate the  $^7\text{Be}$  abun-

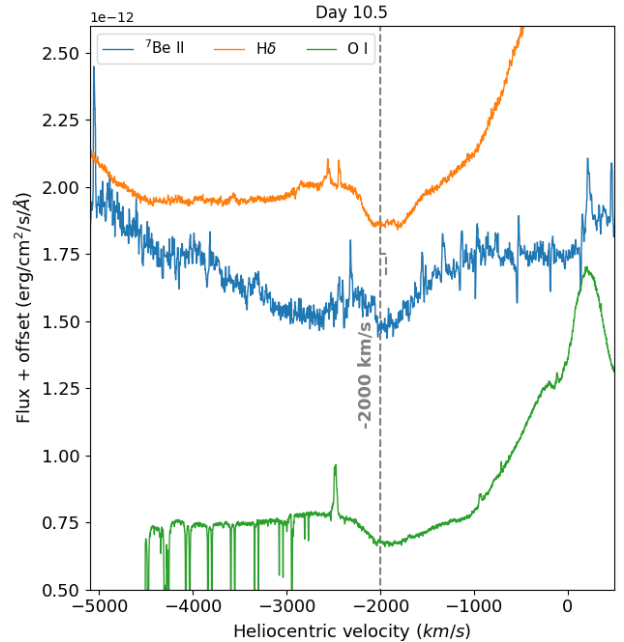


**Figure 8.**  $^7\text{Be}$ , H $\delta$  and O I triplet at 777.19, 777.41 and 777.54 nm spectra at day 10.5 plotted on a common velocity scale. The O I triplet is not resolved though with a separation of  $133 \text{ km s}^{-1}$  and the O I 777.5388 nm wavelength is used for the zero velocity in the plot. Note that the absorption of OI is affected at its left by the emission line of Fe II (73) at 771.2 nm. No other metal elements are detected to check the common absorption system. The narrow absorption features present in the O I spectrum are the telluric lines of the molecular O<sub>2</sub> A band.

dance under the assumption that the two ions are in their main ionization stage. The possibility of overionization of Ca II with respect to  $^7\text{Be II}$  has been discussed in the case of CNe and found unlikely (Molaro et al. 2021). The absorption of the Ca II K line could be seen clearly only at days 1.6 and 2.5, but only in the spectrum taken at day 1.6 is not affected by the nearby emission, so that the  $^7\text{Be}$  abundance could necessarily be derived only at the first epoch.

The equivalent width (EW) of the sum of the  $^7\text{Be II}$  lines is compared with the Ca II K line at 393.366 nm. Following previous analysis we have

$$\frac{N(^7\text{Be II})}{N(\text{Ca II})} = 2.164 \times \frac{EW(^7\text{Be II, Doublet})}{EW(\text{Ca II, K})} \quad (1)$$

with  $\log(gf)$  of -0.178 and -0.479 for the  $^7\text{Be II}$  doublet, and +0.135 for the Ca II K line (Tajitsu et al. 2015; Molaro et al. 2016). The measure of the equivalent width of the main  $^7\text{Be II}$  absorption at  $-2800 \text{ km s}^{-1}$  is performed in a very conservative way in the spectrum of first epoch as shown in Fig. 10 by the shadowed area. The EW of the  $^7\text{Be II}$  doublet is of  $1065 \pm 86 \text{ mÅ}$ . The main uncertainty comes from the continuum placement which is traced here as low as possible. Close to  $^7\text{Be II}$  doublet there are several lines mainly of Cr II and Fe II which could contribute to the observed absorption. However, the close correspondence of the absorption profile assures they are not the dominant species. The equivalent width of the Ca II 393.3 nm line also illustrated in Fig. 10 is of  $859 \pm 116 \text{ mÅ}$ , providing a ratio of  $EW(^7\text{Be II, Doublet})/EW(\text{Ca II, K}) \approx 1.20 \pm 0.2$ . The high

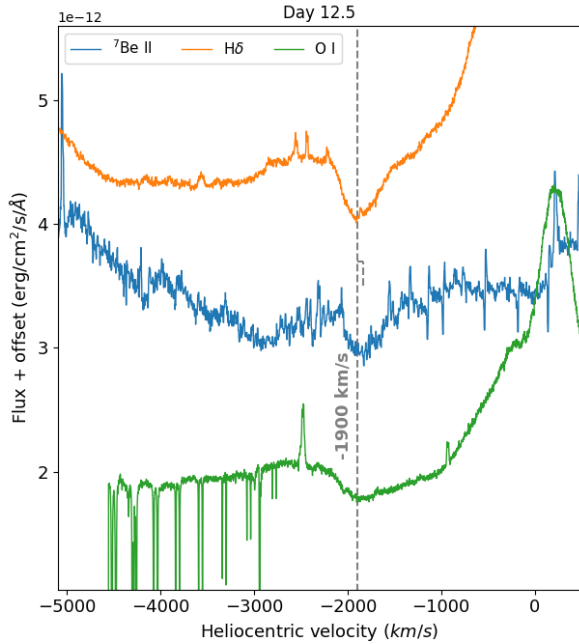


**Figure 9.** As in the previous figure. After this epoch no more absorption is detectable.

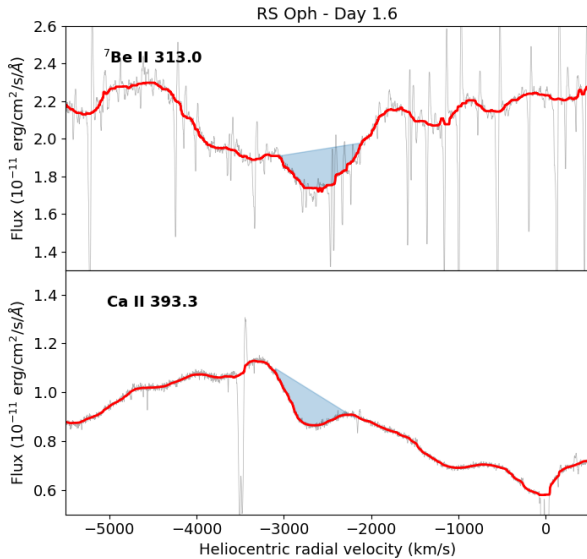


**Figure 10.** The  ${}^7\text{Be II}$  and the  $\text{Ca II K}$  spectra taken at 1.6 d. The red lines show the spectra cleaned from the features of the circumstellar material made by the red giant wind. Highlighted are the conservative measurements of the EWs made by taking the local continuum as low as possible.

**Table 3.** Lines of the red-giant wind in the  ${}^7\text{Be Na I Fe II 430.3 nm}$  and  $\text{H I } \delta$  spectral regions as measured in the spectrum at day 1.6. Some DIBs velocities are also given to emphasize the velocity structure of the interstellar medium towards RS Oph. Velocities are heliocentric with a correction value of  $-21.86 \text{ km s}^{-1}$ . Last column reports the identification number of the lines shown in Fig. 3

ident	abs	fwhm	vel	em	fwhm	ID
Cr II 3136.686	3136.327	0.17	-56.2	3136.663	0.43	1
Fe II 3135.362	3134.992	0.18	-57.3	3135.329	0.51	2
Cr II 3134.303	3133.963	0.11	-54.4	3134.235	0.82	3
Fe II 3133.048	3132.715	0.13	-53.8	3132.999	0.25	4
Cr II 3132.053	3131.662	0.23	-59.3	3132.022	0.79	5
Cr II 3128.700	3128.350	0.17	-58.9	3128.623	0.21	6
Cr II 3124.973	3124.586	0.23	-59.0	3125.004	0.61	7
Cr II 3122.602	3122.259	0.11	-54.7	3122.532	0.25	8
Cr II 3120.369	3119.989	0.18	-58.4	3120.334	0.89	9
Cr II 3118.649	3118.274	0.18	-58.0	3118.621	0.97	10
Fe II 3116.580	3116.221	0.17	-56.5	3116.563	0.44	11
Fe II 3114.683	3114.359	0.13	-53.1	3114.620	0.22	12
Fe II 3114.295	3113.936	0.16	-56.5	3114.177	0.19	13
Sc II 3107.52	3107.235	0.09	-49.3	3107.550	0.59	14
Fe II 3106.565	3106.229	0.13	-54.3	3106.505	0.19	15
Fe II 3105.554	3105.232	0.14	-53.0	3105.502	0.46	16
Fe II 3105.168	3104.813	0.22	-56.2	3105.046	0.13	17
VII 3102.29	3101.971	0.12	-52.7			18
K I 3102.05?	3101.559	0.12	-69.4			18
Fe II 3096.294	3095.937	0.15	-56.5	3096.295	0.42	19
	3093.161	0.09		3093.402	0.22	20
Cr II 3093.17?	3092.773	0.11	-60.4	3092.996	0.23	20
Na I 5889.95095	5889.451	0.07	-47.3			
	5889.151	0.46	-62.6			
	5888.868	0.11	-76.9			
	5889.727	0.07	-33.2			
	5889.903	0.14	-24.3			
	5890.167	0.73	-10.9			
	5890.384	0.35	+0.2			
	5890.533	0.16	+7.8			
H I $\delta$ 4340.472	4339.87	0.43	-63.5	4340.557	0.38	
Fe II 4303.168	4302.672	0.15	-56.5	4303.040	0.50	
DIB 6660.71	6660.870	0.63	-14.7			
DIB 6613.62	6613.865	0.91	-10.8			
DIB 5849.81	5849.914	0.63	-16.5			
DIB 5797.060	5797.268	0.76	-11.1			

velocity component is contaminated by the emission of the hydrogen line and likely the  $\text{Ca II K}$  component is partially filled up by the hydrogen emission. The values of the higher velocity absorption would be of 947 mÅ, and 164 mÅ, respectively, providing a ratio of  $\text{EW}({}^7\text{Be II})/\text{EW}(\text{Ca II}) \approx 4.5$ . We thus consider the ratio from the lower velocity component less affected by blends and more representative of the ratio in all components of the outburst material.

Using Eq. 1, we obtain  $N({}^7\text{Be II})/N(\text{Ca II}) \approx 2.61 \pm 0.43$ . Since the half life time decay of  ${}^7\text{Be}$  is of 53.22 days, after 1.6 days from explosion, the abundance had not significantly reduced assuming the TNR occurred together with the explosion. The abundance of calcium is taken solar  $N(\text{Ca})/N(\text{H}) = 2.19 \pm 0.30 \cdot 10^{-6}$  (Lodders 2019) which gives an abundance of  $N({}^7\text{Be})/N(\text{H}) \approx 5.7 (\pm 1.5) \cdot 10^{-6}$ , or  $X({}^7\text{Be})/X(\text{H}) \approx 4.0 (\pm 1.1) \cdot 10^{-5}$  in mass. Should Calcium abundance be different from solar, the final  $N({}^7\text{Be})/N(\text{H})$  would change accordingly.

### 3.1 Ejected mass

A direct method to estimate the mass of the ejecta consists in deriving it by using the emission intensity of a recombination line together with a good estimate of the electron density in the shell during the nebular phase. A suitable line is  $H_\beta$  and its luminosity at these epochs can be expressed as

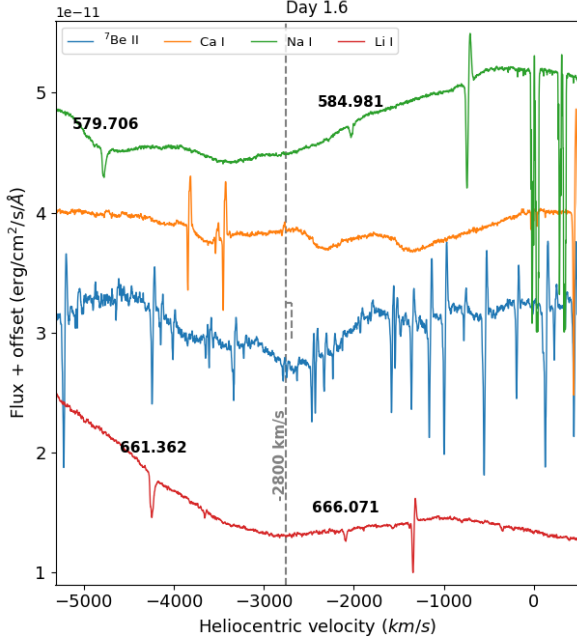


**Figure 11.** Spectrum of RS Oph in the regions of  ${}^7\text{Li I}$  670.8 nm, the D2 line and Na I 589.0 nm and Ca I 422.6 nm. In the portion around  ${}^7\text{Li I}$  670.8 nm the narrow absorptions are due to the DIB 666.071 nm and 661.362 nm while in the Na I region there are the DIBs at 584.981 and 579.706 nm. The P-Cygni lines in the other spectra are due to metal lines arising in the red giant wind. The He I 587.6 nm and He I 667.8 nm are present in the Na I and Li I spectral regions, respectively.

$$L_{H\beta} = 3.03 \cdot 10^{-14} \cdot h\nu \cdot N_e \cdot N_p \cdot V_{ej} \cdot f \quad [\text{erg} \cdot \text{s}^{-1}] \quad (2)$$

where  $3.03 \cdot 10^{-14}$  is the  $H\beta$  effective recombination coefficient (Osterbrock & Ferland 2006),  $h\nu$  is the photon energy,  $N_e$  and  $N_p$  are the electron and proton number densities respectively, while  $V_{ej}$  and  $f$  are the volume and filling factor, respectively. The ejected mass can be written as

$$M_{ej} \approx \mu \cdot m(H) \cdot N_p \cdot V_{ej} \cdot f \quad (3)$$

where  $m(H) = 1.67 \cdot 10^{-24}$  grams and  $\mu \approx 1.4$  is the mean molecular weight.

By combining the two above equations, which has the advantage of cancelling both volume and filling factor, we obtain:

$$M_{ej} = \frac{18.5 \cdot L_{H\beta}}{N_e} \quad (4)$$

We obtained several spectra of the nova at the start of the nebular phase. In Fig. 12, we show the spectrum of 29 March 2022 obtained with UVES. We used a large slit of 3 arcsec to collect all the light ( $\sim 97\%$ ) required to obtain an accurate spectro-photometric flux calibration. The observed flux of  $H\beta$  in the spectrum corrected for reddening  $E(B - V) = 0.73$  (Cassatella et al. 1985; Snijders 1987) is of  $H\beta = 11.5 \cdot 10^{-12} \text{ erg} \cdot \text{s}^{-1} \cdot \text{cm}^{-2}$ . At the distance of 2400 pc it becomes  $L_{H\beta} = 7.95 \cdot 10^{33} \text{ erg} \cdot \text{s}^{-1}$ , and therefore we obtain:

**Table 4.** Nebular Lines used for the estimation of the nova ejecta as measured in the spectrum of 29 March 2022.  $F_c$  is the flux of the continuum adjacent to the emission lines and  $F$  is the total flux of the line above the continuum.

ident	$\lambda_{obs}$ nm	FWHM Å	$F_c$ $\text{erg cm}^{-2}\text{s}^{-1}$	$F$ $\text{erg cm}^{-2}\text{s}^{-1}$
$H\beta$ 486.135	$\approx 485.985$	2.81	$4.9 \cdot 10^{-13}$	$1.15 \cdot 10^{-11}$
He II 468.6571	468.522	2.73	$3.8 \cdot 10^{-13}$	$5.69 \cdot 10^{-12}$
O III 436.3209	436.2199	3.22	$4.2 \cdot 10^{-13}$	$1.24 \cdot 10^{-12}$
O III 495.8911	495.8654	9.23	$3.9 \cdot 10^{-13}$	$5.50 \cdot 10^{-12}$
O III 500.6843	500.6074	9.56	$4.4 \cdot 10^{-13}$	$1.55 \cdot 10^{-11}$

$$M_{ej} = \frac{74.9}{N_e} [M_{\odot}] \quad (5)$$

The electron density in the optical range is generally derived from the ratio of two closely spaced emission lines, e.g. [O II]  $\frac{372.9}{372.6}$  and [S II]  $\frac{671.6}{673.1}$ . Unfortunately, these emission lines are not present in the March spectra. However, the electron density can be derived also from the ratio of the [O III] lines  $\frac{495.9+500.7}{436.3}$ . This ratio is generally a function of both  $T_e$  and  $N_e$ , but for  $N_e$  greater than  $10^4 \text{ cm}^{-3}$  the ratio varies strongly with  $N_e$  because the upper level  ${}^1D_2$  of the 495.9 nm and 500.7 nm lines begins to get collisionally de-excited. Under this condition of high density, the T-Ne diagnostic equation can be represented as (Osterbrock & Ferland 2006):

$$\frac{J_{495.9} + J_{500.7}}{J_{436.3}} = \frac{7.90 \cdot e^{[(3.29 \cdot 10^4)/T_e]}}{1 + 4.5 \cdot 10^{-4} (N_e/T_e^{1/2})} \quad (6)$$

For  $T_e = 10^4 \text{ K}$ , a common value in photoionized nebulae, and inserting the values reported in Tab. 4, the ratio is 16.9 and  $N_e \approx 2.57 \cdot 10^6$ .

This value is rather stable, assuming  $T_e = 10^4 \text{ K}$ , the ejected mass based on  $H\beta$  is of  $M_{ej} \approx 2.9 \cdot 10^{-5} M_{\odot}$ , and a  $T_e = 8 \cdot 10^3 \text{ K}$  would give  $N_e \approx 6.5 \cdot 10^6$ , while a  $T_e = 1.2 \cdot 10^4 \text{ K}$  would give  $N_e \approx 1.4 \cdot 10^6$  corresponding in an uncertainty in the mass of ejecta of about a factor two.

However,  $H\beta$  is found in emission also during quiescence and it is also difficult to separate the contribution of the outburst. The value derived above is more strictly an upper limit to the value of the mass of the ejecta. We have therefore used the He II 468.6 nm which has a certain nebular origin. The equations for He II become:

$$L_{\text{He II}} = 1.58 \cdot 10^{-24} \cdot N_e \cdot N_{\text{He II}} \cdot V_{ej} \cdot f \quad [\text{erg} \cdot \text{s}^{-1}] \quad (7)$$

and

$$M_{\text{He II}} \approx \mu \cdot m(H) \cdot N_{\text{He II}} \cdot V_{ej} \cdot f \quad (8)$$

and we obtain

$$M_{\text{He II}} = \frac{1.5 \cdot L_{\text{He II}}}{N_e} \quad (9)$$

The observed flux of He II 468.6 nm as measured in the spectrum of 29 March 2022 is  $L_{\text{He II}} = 3.0 \cdot 10^{33} \text{ erg} \cdot \text{s}^{-1}$  for a distance of 2.4 Kpc. For  $N_e \approx 2.57 \cdot 10^6$  and considering negligible the presence of He I in the same layers the helium mass is of  $M_{\text{He II}} = 1.73 \cdot 10^{27}$  grams or  $8.7 \cdot 10^{-7} M_{\odot}$  and using a number ratio of H/He = 12.6 we obtain an ejected mass of  $M_{ej} \approx 1.1 \cdot 10^{-5} M_{\odot}$ .

Pandey et al. (2022) estimated of the mass of the ejecta in the 2021



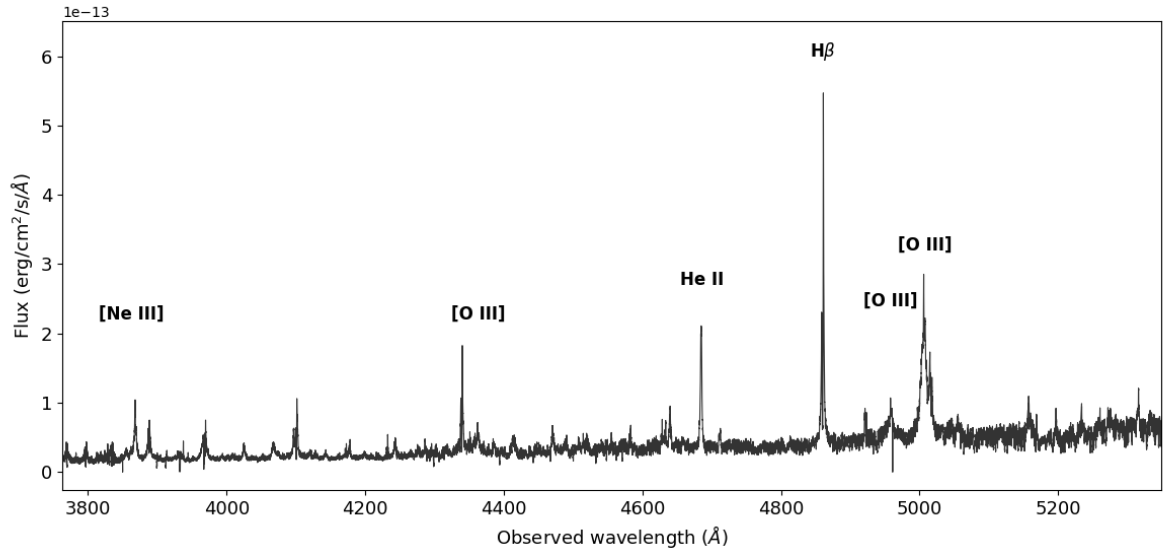


**Figure 12.** The spectrum of RS Oph obtained on 29 March 2022 in the range (380–530) nm. Nebular emission lines are detected on top of a continuum which shows signatures of the red giant atmosphere. The position of the most common ones and the lines used for the estimate of the ejected mass are marked.

outburst with a Cloudy model for the ejecta with hydrogen density, volume and filling factor derived by the best model. These authors estimate the mass of  $M_{ej} \approx 3 - 4 \cdot 10^{-6} M_{\odot}$  but for a distance of 1.68 kpc. By adopting the GAIA distance of 2.4 kpc we are using here the ejecta would be a factor 1.4 higher and about a factor two lower of what derived here.

For the outburst of 2006 Das et al. (2006); Das & Mondal (2015) derived an ejected mass of  $M_{ej} \approx 3 - 5 \cdot 10^{-6} M_{\odot}$ . Modeling the x-ray emission from Chandra observations Orlando et al. (2009) derived  $M_{ej} \approx 10^{-6} M_{\odot}$ . Eyres et al. (2009) derived  $M_{ej} \geq 4 \cdot 10^{-7} M_{\odot}$  and Vaytet et al. (2011)  $M_{ej} \approx 2 - 5 \cdot 10^{-7} M_{\odot}$ . For the outburst of 1985 Anupama & Prabhu (1989) derived a  $M_{ej} \approx 2.3 - 3.7 \cdot 10^{-6} M_{\odot}$ .

An ejected mass of  $\approx 1.1 \cdot 10^{-5} M_{\odot}$  is a relatively high value when compared to the typical ejected material of a RN, and similar to the mass of CNe ejecta, (Della Valle & Izzo 2020). Historical observations of RNe in M31 showed that RNe might be outliers of the Maximum Magnitude vs Rate of Decline (MMRD) relationship (Arp 1956; Rosino 1973). An effective test to verify the mass of the RS Oph ejecta can be performed by studying the position of RS Oph in the MMRD plane. After correction for extinction RS Oph reached  $V = 2.7$  at peak which at the distance of  $d = 2.40 \pm 0.16$  Kpc corresponds to  $M_V \approx -9$ . From the lightcurve shown in Fig. 1 we get  $T_2 = 4.2$  days and a decline of  $\delta V = 0.48$  mag/day. These data show that RS Oph matches well the MMRD of CNe in agreement with our measurement of the RS Oph ejected mass (Della Valle 1991).

We note interesting consequences of such high ejecta. RS Oph is likely to have expelled more material than it has been able to accumulate since the 2006 outburst. Should this be confirmed by the study of previous and future outbursts, it would imply that the WD is eroding during its duty-cycle, thus preventing it from reaching Chandrasekhar mass and exploding as a type-Ia SN.

### 3.2 Lithium

In Fig. 11 the spectrum of RS Oph 1.6 day after explosion is shown in the region of  ${}^7\text{Li I}$  670.8 nm, the D2 line of Na I 589.0 nm and Ca I 422.6 nm. No absorption is detected in correspondence of these neutral species in this and also all other epochs. The narrow absorptions seen in the spectra are due to DIBs while the P-Cygni profile are due to lines originated in the red-giant wind. In particular, there is no evidence of the resonance  ${}^7\text{Li I}$  doublet at 670.8 nm in the spectra of RS Oph as in most classical novae. So far,  ${}^7\text{Li I}$  has been detected only in V1369 Cen (Izzo et al. 2015). The detection in V1369 Cen was determined on days 7 and 13 when only a small amount of  ${}^7\text{Be}$  decayed into  ${}^7\text{Li}$ , which implies that the TNR started much earlier than the explosion (Izzo et al. 2015). Li has been also detected as a trace element in a very early epoch of V906 Car (Molaro et al. 2020) and in V5668 Sgr (Izzo 2019). The equivalent width of the  ${}^7\text{Li}$  line in V5668 Sgr declines with time as the ionization of the ejecta increases and disappears by day 42 after explosion (Wagner et al. 2018). A claim for  ${}^7\text{Li I}$  670.7 nm detection in V382 Vel was made by Della Valle et al. (2002), but Shore et al. (2003) suggested that it could be neutral nitrogen. Neutral  ${}^7\text{Li}$  remains absent from nova outburst spectra also when observations extend to a time scale longer than the  ${}^7\text{Be}$  decay. This is the reason why novae have not been recognized as Li producers for decades after the theoretical suggestion. However, this can be explained if  ${}^7\text{Be}$  decays through the capture of an internal K-electron to end as ionized lithium with transitions only in the X-ray domain (Molaro et al. 2016). The  ${}^7\text{Li I}$  line was discovered in quiescent spectra of RS Oph and T CrB by Wallerstein et al. (2008). The line shows the orbital motion and therefore it is formed in the atmosphere of the red giant (Brandi et al. 2009). The abundance is of  $A(\text{Li}) = 1.1$ , but if we consider the effective temperature and luminosity of this star,  ${}^7\text{Li}$  should have been completely destroyed (see e.g. Lambert et al. 1980; Charbonnel et al. 2020; Magrini et al. 2021, and references therein). This fact was already noted by Wallerstein et al. (2008) both for RS Oph and for T CrB. Although Li-rich giants exist they are rare (see e.g. Kumar et al. 2011; Deepak

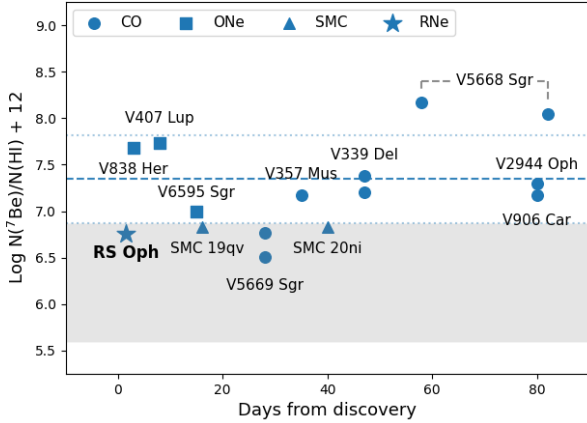


**Figure 13.**  ${}^7\text{Be}$  abundance in RS Oph and in all CNe where it was found. The plot shows in ordinate the  $A({}^7\text{Be}) = \log N({}^7\text{Be})/N(\text{HI}) + 12$ , with  $A({}^7\text{Be}) = 6.76$  for RS Oph. Fast novae are marked with squares, slow novae with circles while MC novae with triangles. The dashed line mark the average value, estimated using only MW novae. To note that the meteoritic abundance is  $A({}^7\text{Li}) = 3.3$  (Lodders et al. 2009).

& Reddy 2019; Martell et al. 2021, and references therein). There is an unsettled debate on whether the  ${}^7\text{Li}$  in Li-rich giants is intrinsic (i.e. produced in the star itself) or extrinsic (i.e. produced elsewhere and then accreted onto the star). Kumar et al. (2020) argued that all stars must undergo a  ${}^7\text{Li}$  production phase between the tip of the Red Giant Branch and the Red Clump. The time spent in this phase is short and only large surveys allow to detect these stars. From the observational point of view we remark that it is surprising that two RNe would show measurable  ${}^7\text{Li}$  in the atmosphere of the cool red giant companion. It is tempting to conjecture that at each outburst a part of the freshly produced  ${}^7\text{Li}$  in the TNR is accreted by the companion star building up and compensating for the destruction due to the convection a measurable amount of  ${}^7\text{Li}$ .

#### 4 DISCUSSION

The possible presence of  ${}^7\text{Be}$  in the outburst spectra of RS Oph adds a member of the class of Recurrent Novae to the small sample of objects where  ${}^7\text{Be}$  has been detected. The  $A({}^7\text{Be})$  yields in RS Oph and the ones measured in the classical novae are compiled in Tab. 5 and are shown in Fig. 13. CNe show a range of different  ${}^7\text{Be}$  yields scattered by one order of magnitude. The scatter exceeds the admittedly large observational errors and is likely real. The light mass of the ejecta and the high terminal velocity is typical of ONe novae but Mikołajewska & Shara (2017) classified RS Oph as a CO nova. However, no difference in the yields between CO and ONe novae is found at variance with theoretical predictions. The mean value is of  $A({}^7\text{Be}) = 7.34 \pm 0.47$  while in RS Oph the abundance is of 6.78 overlapping with the lowest abundances derived in CNe.

Assuming the Li meteoritic abundance as the best proxy for the present Li value in the Galaxy, the current mass of  ${}^7\text{Li}$  can be estimated to be about  $1000 M_{\odot}$  (Starrfield et al. 2020). About 10-25 % of this has been made in the primordial nucleosynthesis and another

10% by the slow spallation processes taking place in the interstellar medium along the whole Galactic life. AGB stars could contribute at most by a few percent (Romano et al. 2001). The astronomical source for the remaining 70% remains to be identified. In fact, the real fraction is even higher considering that about 20-30 percent of Li is burned through recycling within stars.

Detection of significant overabundances of  ${}^7\text{Be}$  in Classical novae, with yields that are about 4 orders of magnitude over the meteoritic  ${}^7\text{Li}$  value (Lodders 2019), makes these systems the more plausible candidates for making the missing Galactic  ${}^7\text{Li}$  fraction. Detailed models of the chemical evolution of the Milky Way showed that novae account well for the observed increase of Li abundance with metallicity in the thin disk, and also for the relative flatness observed in the thick disk (Cescutti & Molaro 2019). In fact, the thick disk evolves on a timescale which is shorter than the typical timescale for the production of substantial  ${}^7\text{Li}$  by novae. Cescutti & Molaro (2019) left the nova yields as a free parameter and found that assuming a nova undergoes explosion every  $10^4$  yr, as suggested by Ford (1978), in order to match the  ${}^7\text{Li}$  growth and the present abundance, a  ${}^7\text{Li}$  production of  $3 \cdot 10^{-9} M_{\odot}$  per nova event is required, which is about what observed.

Detection of  ${}^7\text{Be}$  in recurrent novae as RS Oph provides further support to the suggestion that Novae are the main source of lithium. The ejected mass in the RS Oph 2021 outburst is probably  $\geq 6 \cdot 10^{-6} M_{\odot}$ . With a measured yield in mass of  $X({}^7\text{Be})/X(\text{H}) = 4.0 \cdot 10^{-5}$ , the amount of  ${}^7\text{Li}$  created in the RS Oph 2021 event is of  $\geq 2.4 \cdot 10^{-10} M_{\odot}$ .

Typical RN could have ejecta by one or two order of magnitude smaller than RS OPH and therefore could synthesize something between  $10^{-1}$  to  $10^{-3}$  of the average  ${}^7\text{Li}$  of CNe per event but occur  $10^3$  times more frequently (Ford 1978). The fraction of RNe is difficult to know from observations due to the limited time of astronomical observations and cannot be excluded that some of the nova observed for  ${}^7\text{Be}$  is in fact a RN. In fact, all binaries with a WD are likely recurrent novae with a period which is primarily determined by the mass of the WD and by the mass transfer from the companion. Della Valle & Livio (1996) have estimated for M31 and LMC a fraction RN/CN of 10% and 30%. In the Milky Way a ratio of 12- 35% has been found by Pagnotta & Schaefer (2014) and of 30% by Della Valle & Izzo (2020). Thus, RNe could be one third of the CNe and could concur in making of the  ${}^7\text{Li}$  we observe today in the Milky Way.

#### 5 CONCLUSIONS

- By means of the high resolution UVES spectrograph at the Kueyen-UT2 telescope of the ESO-VLT, Paranal, HARPS-N at the TNG and FIES at the NOT, both in La Palma, Spain, we monitored the 2021 outburst of the recurrent nova RS Oph since day 1.6 from the explosion. Analysis at high resolution in the far blue spectral region enabled detection of the possible presence of  ${}^7\text{Be}$  at 313.0 nm freshly made in the thermonuclear runaway reactions showing that CNe and RNe behave similarly.

- The  ${}^7\text{Be}$  yields can be estimated from the analysis of the first spectrum where the Ca II K line is present and is not affected by the H emission. From the fourth day after the explosion the metal lines are no longer visible in absorption, probably due to the low mass of the ejecta. The yields measured are of  $N({}^7\text{Be})/N(\text{H}) = 5.7 \cdot 10^{-6}$  which are close to the lowest values measured in classical novae.

- By means of spectra taken in the nebular phase we estimate a mass ejecta of  $M_{ej} \approx 1.1 \cdot 10^{-5} M_{\odot}$  providing an amount of  $\approx 4.4 \cdot 10^{-10} M_{\odot}$  of  ${}^7\text{Li}$  created in the 2021 event.

<sup>2</sup>  $A({}^7\text{Be}) = \log N({}^7\text{Be})/N(\text{HI}) + 12$

**Table 5.**  $A(^7\text{Be})$  abundances for the CN and RS Oph.  $N(^7\text{Be})/N(H)_c$  are the values corrected for the  $^7\text{Be}$  decay with a mean life of 76.8 days.

Nova	type	d	comp km s <sup>-1</sup>	$A(^7\text{Be})$	$A(^7\text{Be})_c$	Ref
V339 Del	CO	47	-1103	6.92	7.20	Tajitsu et al. (2015), Tajitsu et al. (2016)
V339 Del	CO	47	-1268	7.11	7.38	Tajitsu et al. (2015), Tajitsu et al. (2016)
V5668 Sgr	CO	58	-1175	7.84	8.17	Molaro et al. (2016)
V5668 Sgr	CO	82	-1500	7.58	8.04	Molaro et al. (2016)
V2944 Oph	CO	80	-645	6.72	7.18	Tajitsu et al. (2016)
V407 Lup	ONe	8	-2030	7.69	7.73	Izzo et al. (2018)
V838 Her	ONe?	3	-2500	7.66	7.68	Selvelli et al. (2018) <sup>1</sup>
V612 Sct	?				-	Molaro et al. (2020)
V357 Mus	CO?	35	≈ -1000	6.96	7.18	Molaro et al. (2020)
FM Cir	CO?				:	Molaro et al. (2020)
V906 Car	CO?	80	≈ -600	6.86	7.30	Molaro et al. (2020)
V5669 Sgr	CO	28	≈ -1000	6.34	6.51	Arai et al. (2021)
V5669 Sgr	CO	28	≈ -2000	6.61	6.77	Arai et al. (2021)
V6595 Sgr	ONe	15	-2700	6.87	6.99	Molaro et al. (2021)
V1369 Cen	CO	7	-550	5.00	5.04	Izzo et al. (2015) <sup>2</sup>
V1369 Cen	CO	13	-560	5.30	5.38	Izzo et al. (2015) <sup>2</sup>
V1369 Cen*	CO	7	-550	4.70	4.78	Izzo et al. (2015) <sup>3</sup>
V1369 Cen*	CO	13	-560	4.78	4.85	Izzo et al. (2015) <sup>3</sup>
SMC ASASSN-19qv	CO	16	-2400	6.62	6.71	Izzo et al. (2022)
SMC ASASSN-20ni	CO?	40	≈ -520	6.41	6.73	Izzo et al. (2022)
RS Oph	NR	1.6	-2800	6.78	6.78	this paper

• RNe of the kind of RS Oph synthesize around the same  $^7\text{Li}$  per event than classical novae, but occur  $10^3$  times more frequently. Recurrent Novae could be one third of classical novae and, therefore, they could have concurred significantly, depending on their ejected mass, to the making of  $^7\text{Li}$  we observe today in the Milky Way. The detection of  $^7\text{Be}$  in RS Oph provides further support to the recent claim that novae are the main source of  $^7\text{Li}$ .

## ACKNOWLEDGMENTS

The observations have been taken under a Target opportunity Program 105.20B6.001, 105.20B6.002 P.I. Paolo Molaro. The ESO staff is warmly acknowledged for the execution of these observations during the pandemic lockdown. Some observations are from the ToO A3TAC20, P.I. L. Izzo and were made with the Italian Telescopio Nazionale Galileo (TNG) operated on the island of La Palma by the Fundación Galileo Galilei of INAF (Istituto Nazionale di Astrofisica) at the Spanish Observatorio del Roque de los Muchachos of the Instituto de Astrofísica de Canarias. Nando Patat is warmly thanked for discussions on the red giant wind and for making available his spectra of RS Oph in quiescence. LI was supported by two grants from VILLUM FONDEN (project number 16599 and 25501). Based on observations made with the Nordic Optical Telescope, owned in collaboration by the University of Turku and Aarhus University, and operated jointly by Aarhus University, the University of Turku and the University of Oslo, representing Denmark, Finland and Norway, the University of Iceland and Stockholm University at the Observatorio del Roque de los Muchachos, La Palma, Spain, of the Instituto de Astrofísica de Canarias. MH acknowledges funding support from the MICIN/AEI grant PID2019-108709GB-I00.

## 6 DATA AVAILABILITY

Based on data from the UVES spectrograph at the Unit 2 of the VLT at the Paranal Observatory, ESO, Chile. ESO data are world-wide available and can be requested after the proprietary period of one year by the astronomical community through the link <http://archive.eso.org/cms/eso-data.html>. They will be shared earlier on reasonable request with the corresponding author.

## REFERENCES

- Anupama G. C., Pavana M., 2020, *Journal of Astrophysics and Astronomy*, **41**, 43
- Anupama G. C., Prabhu T. P., 1989, *Journal of Astrophysics and Astronomy*, **10**, 237
- Arai A., Tajitsu A., Kawakita H., Shinnaka Y., 2021, *ApJ*, **916**, 44
- Arnould M., Norgaard H., 1975, *A&A*, **42**, 55
- Arp H. C., 1956, *AJ*, **61**, 15
- Aydi E., et al., 2020, *ApJ*, **905**, 62
- Bailer-Jones C. A. L., Rybizki J., Fouesneau M., Demleitner M., Andrae R., 2021, *AJ*, **161**, 147
- Bode M. F., Evans A., 2012, *Classical Novae*
- Brandi E., Quiroga C., Mikolajewska J., Ferrer O. E., García L. G., 2009, *A&A*, **497**, 815
- Cameron A. G. W., 1955, *ApJ*, **121**, 144
- Cameron A. G. W., Fowler W. A., 1971, *ApJ*, **164**, 111
- Cassatella A., Hassall B. J. M., Harris A., Snijders M. A. J., 1985, in Burke W. R., ed., *Recent Results on Cataclysmic Variables. The Importance of IUE and Exosat Results on Cataclysmic Variables and Low-Mass X-Ray Binaries*. p. 281
- Cescutti G., Molaro P., 2019, *MNRAS*, **482**, 4372
- Charbonnel C., et al., 2020, *A&A*, **633**, A34
- Cheung C. C., Ciprini S., Johnson T. J., 2021a, *The Astronomer's Telegram*, **14834**, 1

- Cheung C. C., Johnson T. J., Mereu I., Ciprini S., Jean P., 2021b, *The Astronomer's Telegram*, [14845, 1](#)
- Chomiuk L., Metzger B. D., Shen K. J., 2021, *ARA&A*, [59](#)
- Clayton D. D., 1981, *ApJ*, [244, L97](#)
- Cosentino R., et al., 2012, in McLean I. S., Ramsay S. K., Takami H., eds, *Society of Photo-Optical Instrumentation Engineers (SPIE) Conference Series Vol. 8446, Ground-based and Airborne Instrumentation for Astronomy IV*. p. 84461V, [doi:10.1117/12.925738](#)
- Das R., Mondal A., 2015, *New Astron.*, [39, 19](#)
- Das R., Banerjee D. P. K., Ashok N. M., 2006, *ApJ*, [653, L141](#)
- Davids C. N., Laumer H., Austin S. M., 1970, *Phys. Rev. C*, [1, 270](#)
- Deepak Reddy B. E., 2019, *MNRAS*, [484, 2000](#)
- Della Valle M., 1991, *A&A*, [252, L9](#)
- Della Valle M., Izzo L., 2020, *A&ARv*, [28, 3](#)
- Della Valle M., Livio M., 1996, *ApJ*, [473, 240](#)
- Della Valle M., Pasquini L., Daou D., Williams R. E., 2002, *A&A*, [390, 155](#)
- Enoto T., et al., 2021a, *The Astronomer's Telegram*, [14850, 1](#)
- Enoto T., et al., 2021b, *The Astronomer's Telegram*, [14864, 1](#)
- Evans A., Bode F., O'Brien T., Darnley M., 2008, in *RS Ophiuchi (2006) and the Recurrent Nova Phenomenon*.
- Eyres S. P. S., et al., 2009, *MNRAS*, [395, 1533](#)
- Fekel F. C., Joyce R. R., Hinkle K. H., Skrutskie M. F., 2000, *AJ*, [119, 1375](#)
- Ferrigno C., et al., 2021, *The Astronomer's Telegram*, [14855, 1](#)
- Fields B. D., 2011, *Annual Review of Nuclear and Particle Science*, [61, 47](#)
- Ford H. C., 1978, *ApJ*, [219, 595](#)
- Friedjung M., 1979, *A&A*, [77, 357](#)
- Gaia Collaboration et al., 2021, *A&A*, [649, A1](#)
- Gallagher J. S., Starrfield S., 1978, *ARA&A*, [16, 171](#)
- Gomez-Gomar J., Hernanz M., Jose J., Isern J., 1998, *MNRAS*, [296, 913](#)
- H. E. S. S. Collaboration et al., 2022, arXiv e-prints, [p. arXiv:2202.08201](#)
- Hachisu I., Kato M., 2001, *ApJ*, [558, 323](#)
- Harris M. J., Teegarden B. J., Weidenspointner G., Palmer D. M., Cline T. L., Gehrels N., Ramaty R., 2001, *ApJ*, [563, 950](#)
- Hernanz M., José J., 2008, *New Astron. Rev.*, [52, 386](#)
- Hernanz M., Jose J., Coc A., Isern J., 1996, *ApJ*, [465, L27](#)
- Izzo L., 2019, in Griffin R. E., ed., Vol. 339, *Southern Horizons in Time-Domain Astronomy*. pp 61–64, [doi:10.1017/S1743921318002223](#)
- Izzo L., et al., 2015, *ApJ*, [808, L14](#)
- Izzo L., et al., 2018, *MNRAS*, [478, 1601](#)
- Izzo L., et al., 2022, *MNRAS*, [510, 5302](#)
- Jean P., Hernanz M., Gómez-Gomar J., José J., 2000, *MNRAS*, [319, 350](#)
- José J., Hernanz M., 1998, *ApJ*, [494, 680](#)
- Kafka S., 2021, <https://www.aavso.org>
- Kato M., Hachisu I., 2012, *Bulletin of the Astronomical Society of India*, [40, 393](#)
- Kumar Y. B., Reddy B. E., Lambert D. L., 2011, *ApJ*, [730, L12](#)
- Kumar Y. B., Reddy B. E., Campbell S. W., Maben S., Zhao G., Ting Y.-S., 2020, *Nature Astronomy*, [4, 1059](#)
- Lambert D. L., Dominy J. F., Sivertsen S., 1980, *ApJ*, [235, 114](#)
- Lindgren L., et al., 2021, *A&A*, [649, A4](#)
- Livio M., Truran J. W., 1992, *ApJ*, [389, 695](#)
- Lodders K., 2019, arXiv e-prints, [p. arXiv:1912.00844](#)
- Lodders K., Palme H., Gail H.-P., 2009, *Landolt Börnstein*,
- Luna G. J. M., et al., 2021, *The Astronomer's Telegram*, [14872, 1](#)
- MAGIC Collaboration et al., 2022, arXiv e-prints, [p. arXiv:2202.07681](#)
- Magrini L., et al., 2021, *A&A*, [651, A84](#)
- Martell S. L., et al., 2021, *MNRAS*, [505, 5340](#)
- Mikołajewska J., Shara M. M., 2017, *ApJ*, [847, 99](#)
- Molaro P., Izzo L., Mason E., Bonifacio P., Della Valle M., 2016, *MNRAS*, [463, L117](#)
- Molaro P., Izzo L., Bonifacio P., Hernanz M., Selvelli P., della Valle M., 2020, *MNRAS*, [492, 4975](#)
- Molaro P., et al., 2021, arXiv e-prints, [p. arXiv:2111.01469](#)
- Montez R. J., Luna G. J. M., Mukai K., Sokoloski J., Kastner J. H., 2021, arXiv e-prints, [p. arXiv:2110.04315](#)
- Munari U., Valisa P., 2021, arXiv e-prints, [p. arXiv:2109.01101](#)
- Orlando S., Drake J. J., Laming J. M., 2009, *A&A*, [493, 1049](#)
- Osterbrock D. E., Ferland G. J., 2006, *Astrophysics of gaseous nebulae and active galactic nuclei*
- Page K. L., 2021, *The Astronomer's Telegram*, [14894, 1](#)
- Page K. L., Osborne J. P., Aydi E., 2021, *The Astronomer's Telegram*, [14848, 1](#)
- Pagnotta A., Schaefer B. E., 2014, *ApJ*, [788, 164](#)
- Pandey R., Habbie G. R., Bandyopadhyay R., Das R., Teyssier F., Guarro Flo J., 2022, arXiv e-prints, [p. arXiv:2207.10473](#)
- Patat F., Chugai N. N., Podsiadlowski P., Mason E., Melo C., Pasquini L., 2011, *A&A*, [530, A63](#)
- Pizzuto A., Vandenbroucke J., Santander M., IceCube Collaboration 2021, *The Astronomer's Telegram*, [14851, 1](#)
- Ribeiro V. A. R. M., et al., 2009, *ApJ*, [703, 1955](#)
- Romano D., Matteucci F., Ventura P., D'Antona F., 2001, *A&A*, [374, 646](#)
- Rosino L., 1973, *A&AS*, [9, 347](#)
- Rout S. K., Srivastava M. K., Banerjee D. P. K., Vadawale S., Joshi V., Kumar V., 2021, *The Astronomer's Telegram*, [14882, 1](#)
- Rupen M. P., Mioduszewski A. J., Sokoloski J. L., 2008, *ApJ*, [688, 559](#)
- Schachter J., 1991, *PASP*, [103, 457](#)
- Schaefer B. E., 2010, *ApJS*, [187, 275](#)
- Selvelli P., Cassatella A., Gilmozzi R., González-Riestra R., 2008, *A&A*, [492, 787](#)
- Selvelli P., Molaro P., Izzo L., 2018, *MNRAS*, [481, 2261](#)
- Shidatsu M., et al., 2021, *The Astronomer's Telegram*, [14846, 1](#)
- Shore S. N., et al., 2003, *AJ*, [125, 1507](#)
- Siebert T., et al., 2018, *A&A*, [615, A107](#)
- Siebert T., Ghosh S., Mathur K., Spraggon E., Yeddapanudi A., 2021, arXiv e-prints, [p. arXiv:2104.00363](#)
- Snijders M. A. J., 1987, *Ap&SS*, [130, 243](#)
- Sokolovsky K., Aydi E., Chomiuk L., Kawash A., Strader J., Mukai K., Li K.-L., 2021a, *The Astronomer's Telegram*, [14535, 1](#)
- Sokolovsky K., et al., 2021b, *The Astronomer's Telegram*, [14886, 1](#)
- Starrfield S., Truran J. W., Sparks W. M., Arnould M., 1978, *ApJ*, [222, 600](#)
- Starrfield S., Bose M., Iliadis C., Hix W. R., Woodward C. E., Wagner R. M., 2020, *ApJ*, [895, 70](#)
- Taguchi K., Kawabata M., Yamanaka M., Isogai K., 2021, *The Astronomer's Telegram*, [14513, 1](#)
- Tajitsu A., Sadakane K., Naito H., Arai A., Aoki W., 2015, *Nature*, [518, 381](#)
- Tajitsu A., Sadakane K., Naito H., Arai A., Kawakita H., Aoki W., 2016, *ApJ*, [818, 191](#)
- Tatischeff V., Hernanz M., 2007, *ApJ*, [663, L101](#)
- Telting J. H., et al., 2014, *Astronomische Nachrichten*, [335, 41](#)
- Vaytet N. M. H., O'Brien T. J., Page K. L., Bode M. F., Lloyd M., Beardmore A. P., 2011, *ApJ*, [740, 5](#)
- Wagner S. J., H. E. S. S. Collaboration 2021a, *The Astronomer's Telegram*, [14844, 1](#)
- Wagner S. J., H. E. S. S. Collaboration 2021b, *The Astronomer's Telegram*, [14857, 1](#)
- Wagner R. M., Woodward C. E., Starrfield S., Ilyin I., Strassmeier K., 2018, in *American Astronomical Society Meeting Abstracts #231*. p. 358.10
- Wallerstein G., Harrison T., Munari U., Vanture A., 2008, *PASP*, [120, 492](#)